ROLE OF THE VERTICAL PRESSURE GRADIENT IN WAVE BOUNDARY LAYERS

Karsten Lindegård Jensen[1], B. Mutlu Sumer[1], Giovanna Vittori[2] and Paolo Blondeaux[2]

The pressure field in an oscillatory boundary layer is obtained by means of direct numerical simulations (DNS). The vertical pressure gradient is treated as any other turbulence quantity and its statistical properties are calculated from the DNS data. Moreover, a criterion involving the vertical pressure gradient is used to detect spots. The large fluctuations of the vertical pressure gradient, which take place in the turbulent flow, have significant implications for sediment transport.

Keywords: *wave boundary layers, turbulence, vertical pressure gradient, DNS, transition to turbulence*

INTRODUCTION

Wave boundary layers have been studied extensively over the past decades. The studies cover the entire range of flow regimes: laminar, transitional and turbulent regimes. Observations show that, in the transitional regime, turbulence first emerges in isolated areas where the flow "bursts" with violent oscillations (Carstensen, Sumer and Fredsøe, 2010). These areas, which are called "turbulent spots", and they grow in time, and once they merge, the flow becomes fully turbulent. Carstensen et al's. (2010) work was later extended to the case of solitary wave boundary layers (Sumer et al, 2010) and wave boundary layers over a rough bed (Carstensen, Sumer and Fredsøe, 2012).

Mazzuoli, Vittori and Blondeaux (2011) have recently simulated the dynamics of turbulent spots in wave boundary layers by means of Direct Numerical Simulation (DNS) and reproduced the experimental results by Carstensen et al. (2010) to complement their results.

In the present study the same DNS data as in Test 1 of Mazzuoli et al. (2011) are examined in terms of vertical pressure gradient, presumably a new quantity in the analysis of turbulent wave boundary layers.

This new approach and the interpretation of the DNS results shed a new light onto the laminar-to-turbulent transition in wave boundary layers and the dynamics of sediment grains in the transitional regime.

NUMERICAL MODEL

Applying the linear Stokes wave theory, the orbital motion of the water particles near the seabed turn out to be parallel to it. Introducing a Cartesian coordinate system (x_1^*, x_2^*, x_3^*), such that x_1^* is in the direction of the wave propagation, x_2^* is vertical and x_3^* points in the spanwise direction (see Fig. 1), the flow in the boundary layer can be studied as an oscillatory flow driven by a pressure gradient given by

$$\frac{\partial P^*}{\partial x_1^*} = -\rho^* U_{0m}^* \omega^* \sin(\omega^* t^*)\,; \quad \frac{\partial P^*}{\partial x_2^*} = 0; \quad \frac{\partial P^*}{\partial x_3^*} = 0 \tag{1}$$

where U_{om}^* and $\omega^* = 2\pi/T^*$ are the amplitude and the angular frequency of the fluid oscillations and T^* is the period. As in Blondeaux and Vittori (1994), Costamagna et al. (2003) and Mazzuoli et al. (2011), the bottom profile has a small waviness in the x_1^*- and x_3^*-directions, and the vertical coordinate x_2^* is measured from the mean wall (or bed) level. The waviness of the bottom profile η^* is generated by the superimposition of sinusoidal components and is described by

[1] Technical University of Denmark, Department of Mechanical Engineering, Section for Fluid Mechanics, Coastal and Maritime Engineering, 2800 Kgs. Lyngby, Denmark

[2] University of Genoa, Department of Civil, Chemical and Environmental Engineering, Via Montallegro 1, 16146 Genoa, Italy

$$x_2^* = \epsilon^* \eta(x_1^*, x_3^*) = \epsilon^* \sum_{n=1}^{N} a_n \cos(\alpha_n^* x_1^* + \gamma_n^* x_3^* + \phi_n) \tag{2}$$

where $\epsilon^* a_n$ is the amplitude of the nth-harmonic component. In the present simulation ϵ^* is equal to $0.005\delta^*$, (δ^* being the Stokes length $= \sqrt{2\nu^*/\omega^*}$ and ν^* the kinematic viscosity of sea water). The components of the waviness are characterized by wave numbers α_n^* and γ_n^* in the x_1^* and x_3^* directions, respectively, and a phase shift ϕ_n. Vittori and Verzicco (1998) investigated the effect of the wall waviness and found that the wall waviness is necessary to trigger transition to the intermittently turbulent regime, even if its amplitude is so small that it has no significant influence on turbulence characteristics and the wall can be considered smooth from a macroscopic point of view.

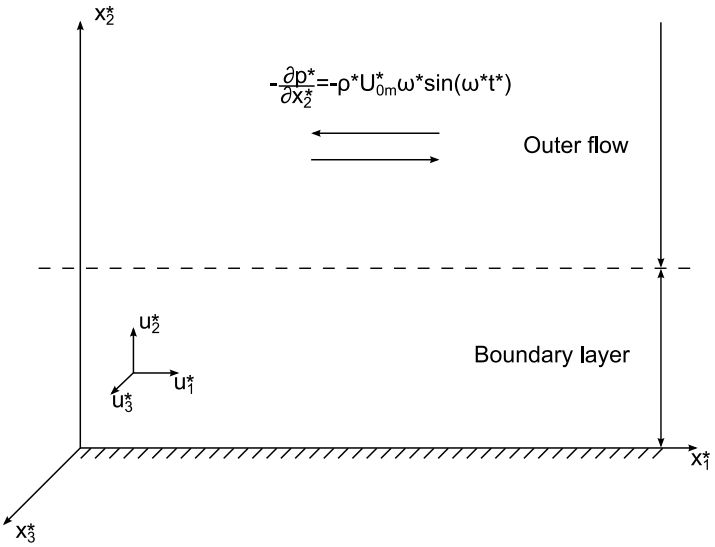

Figure 1. Definition. The outer flow is driven by a pressure gradient in the streamwise direction.

The non-dimensional form of the Navier-Stokes equation reads

$$\frac{\partial u_i}{\partial t} + \frac{R_\delta}{2} u_j \frac{\partial u_i}{\partial x_j} = -\frac{R_\delta}{2} \frac{\partial p}{\partial x_i} - \delta_{i1} \sin(t) + \frac{1}{2} \frac{\partial^2 u_i}{\partial x_k \partial x_k} \qquad for\ i = 1, 2, 3 \tag{3}$$

and continuity equation becomes

$$\frac{\partial u_i}{\partial x_i} = 0 \quad \text{for } i = 1, 2, 3 \tag{4}$$

where the following non-dimensional variables are used

$$\begin{aligned} t &= t^* \omega^*; \quad (x_1, x_2, x_3) = \frac{(x_1^*, x_2^*, x_3^*)}{\delta^*} \\ p^* &= \frac{p^*}{\rho^* U_{0m}^{*2}}; \quad (u_1, u_2, u_3) = \frac{(u_1^*, u_2^*, u_3^*)}{U_{0m}^*} \end{aligned} \tag{5}$$

where t^* is the time, p^* is the pressure, u_i^* is the velocity component in the x_i^* direction, $R_\delta = U_{0m}^*\delta^*/\nu^*$ is the Reynolds number, based on the Stokes length δ^*.

Eqs. 3 and 4 are solved numerically in a computational domain, the size of which is L_{x1}, L_{x2} and L_{x3} in the streamwise, the vertical and the spanwise directions, respectively (see Table 1). At the bottom, the no-slip condition is enforced. Since the wall waviness is assumed to be much smaller than the thickness of the laminar boundary layer ($\epsilon = \epsilon^*/\delta^* \ll 1$), the no-slip boundary condition is expanded up to second order in the variable ϵ and is forced at $x_2 = 0$ (Mazzuoli et al., 2011). Since the accuracy of the numerical method employed to solve the Navier Stokes equation is of second order and ϵ is smaller than the size of the first computational grid in the vertical direction, there is consistency between the numerical scheme and boundary condition (Vittori and Verzicco, 1998).

At the upper boundary ($x_2 = L_{x2}$) a symmetry condition is applied which is equivalent to force the vanishing of the tangential stresses far from the bed. Finally periodicity is enforced along the x_1^*- and x_3^*- axes, because the turbulent flow is assumed to be homogeneous along these directions.

The mesh is uniform in the x_1 and x_3 directions and non-uniform in the x_2 direction so that the grid points are clustered near the bed (minimum grid size is $0.16\delta^*$ and maximum grid size is $0.59\delta^*$). The method uses second order finite difference approximations for the spatial derivatives and the fraction-step method for the time derivatives in the Navier-Stokes equation. For a more detailed description of the numerical procedure, see Kim and Moin (1985), Orlandi (1989), Vittori and Verzicco (1998) and Costamagna et al. (2003).

Table 1. Numerical parameters for the test. Here $\alpha_n = \alpha_n^*\delta^*$ and $\gamma_n = \gamma_n^*\delta^*$.

test	R_δ	Re	L_{x1}	L_{x2}	L_{x3}	n_1	n_2	n_3
1	948	$4.5 \cdot 10^5$	213.6	25.13	75.40	541	65	385
test	a_2	a_2	α_1	α_2	γ_1	γ_2	ϕ_1	ϕ_2
1	1	0.1	0.5	0	0	1	0	0

The test conditions and the properties of the numerical mesh are given in Table 1. In Table 1 $\mathrm{Re} = U_{0m}^* a^*/\nu^*$, where $a^* = U_{0m}^* T^*/(2\pi)$, n_1, n_2 and n_3 are the number of grid points in streamwise, vertical and spanwise direction, respectively.

The computational domain should be large enough to contain the largest coherent vortex structure that occurs in the boundary layer and, simultaneously the grid size should be small enough to describe the smallest turbulent eddies. To secure these conditions a fast Fourier transform of the velocity field has been performed and it has been verified that the amplitude of the spectral components with the largest and smallest wave numbers are smaller than a few percent of the maximum amplitude.

Turbulent spots. Laminar-to-turbulent transition

Turbulent spots are isolated areas in an otherwise laminar flow where the flow "bursts" into violent random oscillations, first observed by Carstensen et al. (2010) for the wave boundary layers. These observations were complemented by the DNS simulations of turbulent spots in oscillatory boundary layers by Mazzuoli et al. (2011) and Mazzuoli (2013).

Turbulent spots can be visualized in CFD experiments by various criteria involving "traditional" turbulence quantities such as turbulent kinetic energy production (TKEP ($-\overline{u_i'u_j'}\partial\overline{u_i}/\partial x_j$)), turbulent kinetic energy (TKE ($1/2\overline{u_i'u_i'}$)), wall-shear-stress fluctuations, or velocity fluctuations (an overbar denotes the ensemble average). Fig. 2a displays the contour plot of the TKEP at a distance $x_2 = 0.24$ from the wall at $\omega t = 45\,°$ (the flow being from left to right) and shows that, turbulent spots can be visualized by the larger values of TKEP. Fig. 2a is accompanied by another contour plot (Fig. 2b),

namely the contour plot of the quantity $-\partial p/\partial x_2$, i.e. the pressure gradient in the direction perpendicular to the wall at the same x_2 location and phase as in Fig. 2a:

$$-\frac{\partial p}{dx_2} = -\frac{\delta^*}{\rho^* U_{0\mathrm{m}}^{*2}} \frac{\partial p^*}{\partial x_2^*} \tag{6}$$

Note that the vertical distance $x_2 = 0.24$ (at which these contour plots are given) is the level closest to the wall where the vertical pressure gradient can be resolved in the present DNS simulation.

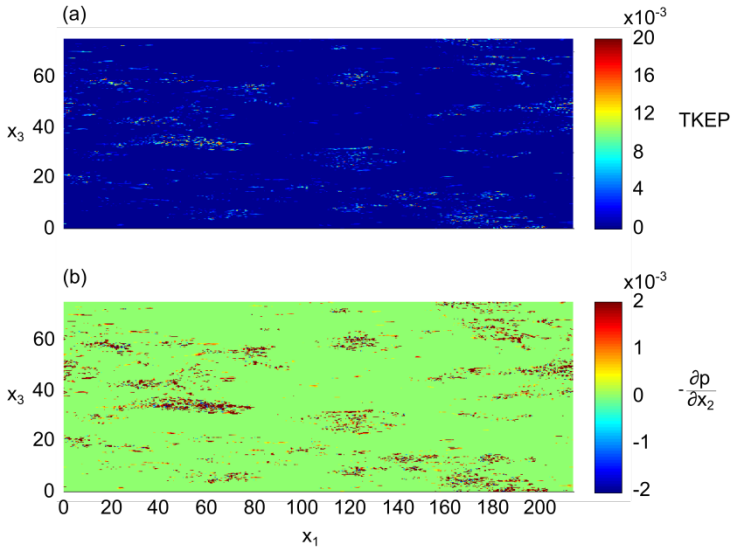

Figure 2.Turbulent spots at ωt = 45° visualised using (a): the turbulent kinetic energy production (TKEP) as Mazzuoli et al. (2011). (b): the vertical pressure gradient. The flow is from left to right. Qualitatively the two criteria (namely, the vertical pressure gradient and the turbulent kinetic energy production (TKEP)) are capable of detecting the same areas where the flow becomes turbulent .

We also note that, for convenience, the minus sign is added to $\partial p/\partial x_2$ so that a positive value of $(-\partial p/\partial x_2)$ indicates an upward-directed force on fluid particles. As shown by Fig. 2, the turbulent spots, visualized by the vertical pressure gradient (Fig. 2b), are strikingly similar to those visualized by the TKEP (Fig. 2a).

The DNS simulation indicates that turbulent fluctuations appear simultaneously at multiple locations in the $(x_{,1}\, x_3)$-plane. When they first occur, they are rapidly damped. Later, however, around $\omega t = 20°$, they begin to remain sustained, and turbulent spots emerge. Then, the spots grow in size until they merge whereby the entire near bed region becomes turbulent at $\omega t = 65°$. These DNS simulations are in qualitative and to some degree quantitative agreement with the measurements of Jensen et al. (1989) and Carstensen et al. (2010) although the DNS results imply an early transition by $\mathrm{O}(30 - 40°)$. This might be related to (a) the difficult and possible subjective judgments in defining the transition limit in the experiments, (b) the higher level of the disturbances in the experimental apparatus compared to that of the numerical simulations.

Statistical analysis of the vertical pressure gradient

The analysis of the previous section clearly shows that the quantity $(-\partial \mathrm{p}/\partial \mathrm{x}_2)$ can describe the laminar-to-turbulent transition rather well, indeed as good as, for example, the turbulent kinetic energy production. This result stimulated the study of the statistical properties of the vertical pressure gradient,

$(-\partial \mathrm{p}/\partial \mathrm{x}_2)$. Presently the the mean value and the standard deviation are calculated from the data obtained by means of the DNS results. The analysis is presented in three steps: (1) Bed shear stress; (2) Turbulence quantities; and (3) Vertical pressure gradient. The first two steps are included in the analysis as they prove to be useful for the analysis of the pressure gradient, i.e. the focus of the present study

.

Bed shear stress

Fig. 3 displays the time variation of the phase resolved mean bed shear stress $\overline{\tau_0}$ (averaged over the entire (x_1, x_3)-plane) where $\tau^* = \mu^* \partial u_1^*/\partial x_2^*$, and τ_0 is its value at $x_2^* = 0$

$$\frac{\overline{\tau_0^*}\delta^*}{\mu^* U_{0m}^*} = \overline{\tau_0} = \left.\frac{\partial u_3}{\partial x_2}\right|_{x_2=0} \tag{7}$$

As seen from Fig. 3, the bed shear stress leads the free stream by a phase difference of 20°. This agrees well with the experimental data reported in Jensen et al. (1989) and Carstensen et al. (2010).

The maximum value of the bed shear stress obtained in the present simulation is $\overline{\tau_0} = 1.9$. Using this value and considering $T^* = 9.72$s, the wave friction factor defined by

$$f_w = 2\frac{\overline{\tau}_{0m}^*}{\rho^* U_{0m}^{*2}} \tag{8}$$

is found to be $f_w = 0.075$. The latter value matches the results from Spalart and Baldwin (1987), but higher than the experimental data from Jensen et al.'s (1989), namely $f_w \cong 0.004$.

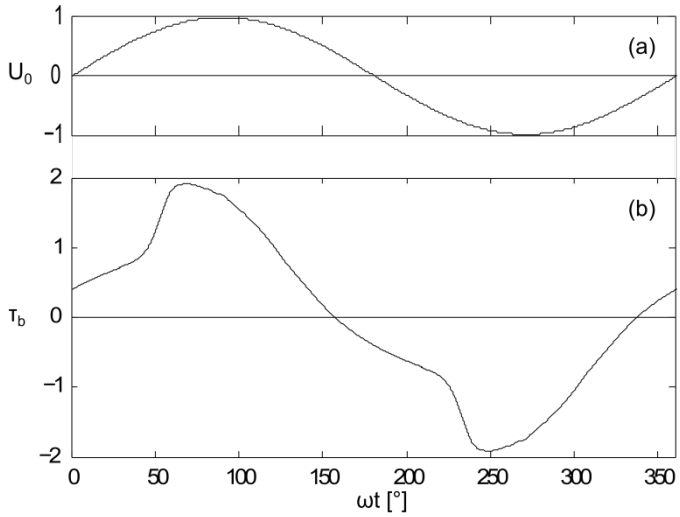

Figure 3. a: The normalized free stream velocity. b: The normalized bed shear in terms of bed friction velocity.

Turbulence quantities

Figs. 4 and 5 show the time development of the vertical profiles of different turbulence quantities, namely $\left(\overline{u_i'^2}\right)^{1/2}$ $(i = 1, 2, 3)$ and $\overline{u_1' u_2'}$ where u_i' is the non-dimensional fluctuating component of the

velocity u_i. A direct comparison of the present numerical results with the results of Spalart and Baldwin (1987) and Jensen et al. (1989) reveals a fair agreement even though no figure of this comparison is presently shown for the sake of space.

The time development of the turbulence quantities is shown in Fig. 4 by showing four selected phase values, namely $\omega t = 0°, 45°, 90°$ and $135°$. At the reversal of the free stream flow ($\omega t = 0°$), turbulence has spread over a substantial portion of the boundary layer, up to a height of $x_2 \cong 14$. By the time the phase reaches $\omega t = 45°$ (Panel b), this turbulence is dissipating, and it is only close to the bed that turbulence production takes place again and new a peak in the r.m.s. values of u_1' appears. As the phase value increases further ($\omega t = 90°$, Panel c) the buildup of turbulence continues in all three velocity components. Finally, at $\omega t = 135°$ (Panel d) the turbulence production stops and turbulence spreads out far from the wall up to $x_2 \cong 12$. This continuous buildup of turbulence is due to diffusion effects that make the boundary layer thickness to grow during the entire wave cycle until a new boundary layer starts to form near bed at flow reversal (Jensen et al. 1989).

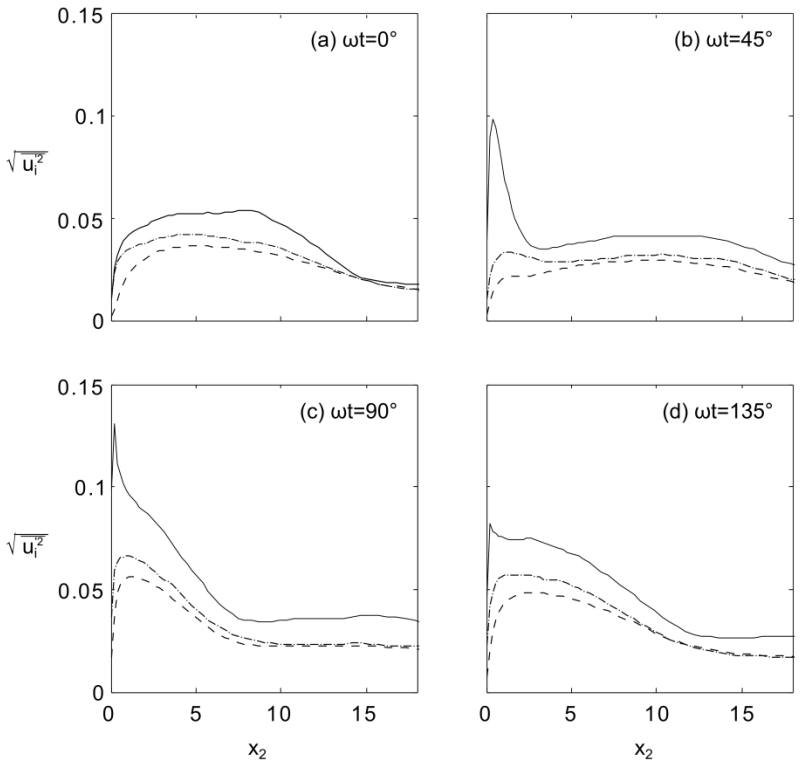

Figure 4. Time evolution of turbulence quantities. R.m.s. values of u_i' for selected phases. —— u_1', – – u_2' and —·— u_3'

A similar time development is found for the non-dimensional Reynolds stresses which are shown in Fig. 5. In Fig. 5a, the Reynolds stresses from the previous period are not yet dissipated. The negative values, which are present in Fig. 5a, are due to the effect of the flow reversal. In Fig. 5b, the turbulence produced during the previous half cycle is dissipating and a new buildup starts near the bed. Panels Fig. 5c and Fig. 5d show that the buildup continues until the flow reverses, in exactly the same fashion as in Fig. 4. The results presented in Figs. 4 and 5 are in full agreement with Jensen et al.'s (1989) measurements. Furthermore, although not shown here for the sake of space, the present results for $\omega t = 90°$ are in agreement with the steady boundary layer data. This is an expected result, as the

oscillatory boundary layer behaves much the same as the steady boundary layer since at this phase the streamwise pressure gradient driving the oscillatory boundary layer becomes rather small (and indeed it vanishes at $\omega t = 90°$).

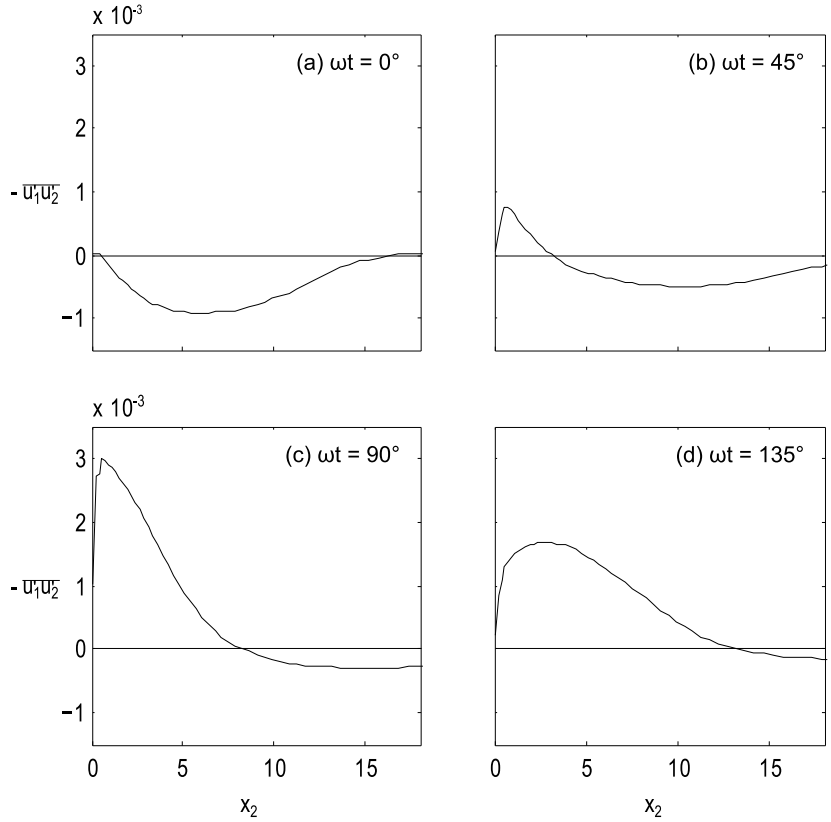

Figure 5. Time evolution of Reynolds stresses $\overline{u_1' u_2'}$ for selected phases.

Vertical pressure gradient

Fig. 6 shows the time development of the non-dimensional vertical profiles of the vertical pressure gradient $\overline{\partial p/\partial x_2}$ for the same phases as in Figs. 4 and 5. Similar to the turbulence quantities in Figs. 4 and 5, the pressure gradient is normalized by the outer flow parameters (Eq. 6), i.e. the maximum free stream velocity and the density of the fluid. Moreover, the average (overbar) is taken over the entire plane (x_1, x_3)-plane, as for the other turbulence quantities.

Two sets of data are plotted in Fig. 6. The first one (the solid lines in the figure) represents the conditional averaged vertical pressure gradient corresponding to $-\partial p/\partial x_2 > 0$ (the upward-directed pressure gradient), while the second set of data (the broken lines in the figure) represents the conditional averaged vertical pressure gradient corresponding to $-\partial p/\partial x_2 < 0$ (the downward-directed pressure gradient).

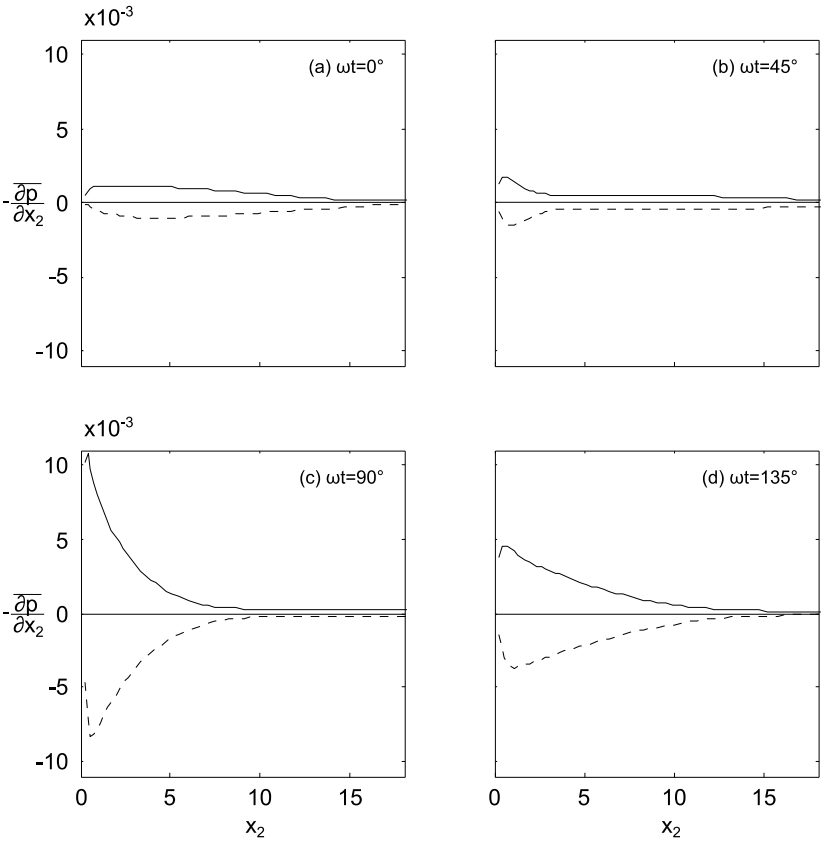

Figure 6. Conditional averaged value of $-\partial p/\partial x_2$ for selected phase values. —— $(-\partial p/\partial x_2 > 0)$ **and – –** $(-\partial p/\partial x_2 < 0)$**.**

The condition described in the previous paragraph implies that, for upward directed pressure gradients, the fluid particles with zero vertical momentum tend to move upward, and vice versa. However for fluid particles with finite vertical momentum, first the aforementioned vertical pressure gradient is used to "consume" the momentum of the fluid particles, before the particles begin to move in the direction dictated by the vertical pressure gradient.

First of all, Fig. 6 shows that, regardless of the phase value, the vertical pressure gradient $\overline{-\partial \mathrm{p}/\,\partial \mathrm{x}_2}$ appears to be largest very near the bed, in the region associated to the generation of turbulence, $x_2 = \mathrm{O}(1)$. Moreover, Fig. 6 shows that $\overline{-\partial \mathrm{p}/\partial \mathrm{x}_2}$ increases tremendously with increasing phase, attaining very large values a $\omega t = 90°$ before it begins to fall off. A third observation from Fig. 6 is that the upward-directed pressure gradient appears to be larger than the downward-directed pressure gradient, and this appears to be the case throughout the phase space. It is likely that strong vertical pressure gradients are introduced by turbulent coherent vortex structures and our future work will be devoted to verify this conjecture

At this stage, it is interesting to compare the time development of the vertical pressure gradient (Fig. 6) with the time development of the other turbulence quantities (Figs. 4 and 5). When inspected closely, Figs 4 and 5 show that turbulence is generated in a region close to the wall where $x_2 = \mathrm{O}(1)$. Then, turbulence is constantly fed into the main body of the flow, by its spreading across the boundary layer up to heights as large as $x_2 \cong 15$. This "diffusion" of turbulence across the boundary layer is rather clear, even at $\omega t = 0°$ when there is a substantial amount of turbulence left from the previous half

cycle (Fig. 4, Panel a), as also revealed by Jensen's work (1989). This behaviour cannot be observed in the time development of the pressure-gradient (Fig. 6), because the dynamics of the pressure gradient is not controlled by diffusive effects.

The present results reveal that the chain of events occurs as described in the following. First, the vertical pressure gradient is generated (practically momentarily) near the bed, and this causes fluid motion in the vertical direction (upwards or downwards depending on the direction of the pressure gradient). This is essentially the turbulence, and it is known that the turbulent kinetic energy generated this way (represented by $k = \overline{u_i u_i}/2$ a scalar quantity) is governed by a diffusion process, revealed by Fig. 4.

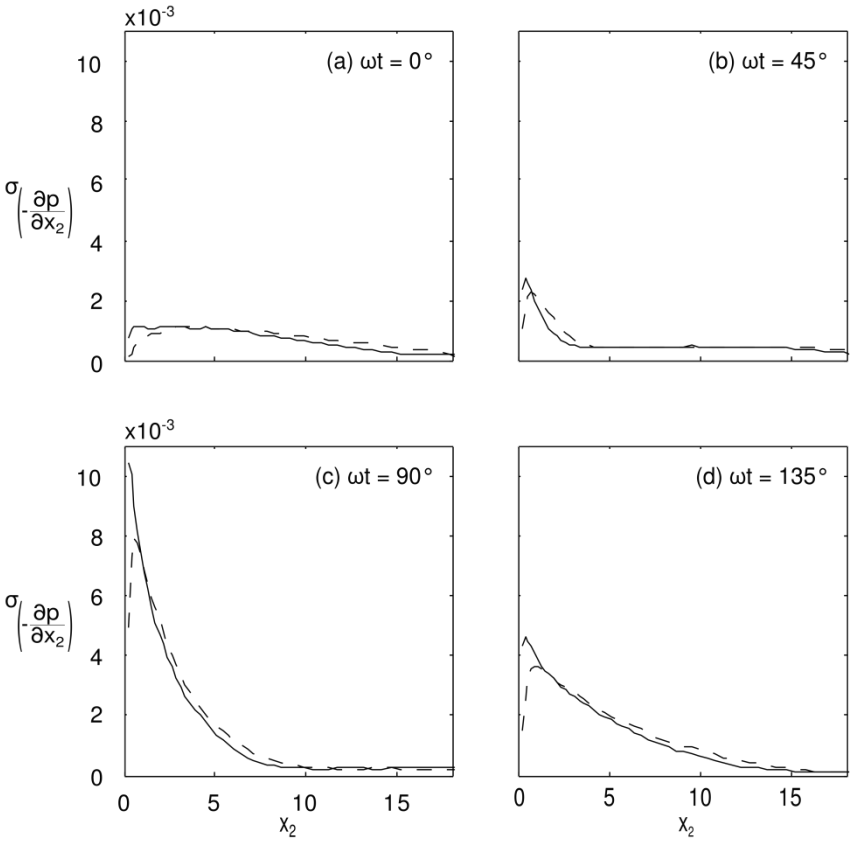

Figure 7. Standard deviation of the conditional averaged value of $-\partial p/\partial x_2$ for selected phase values. —— $\sigma(-\partial p/\partial x_2 > 0)$ and — — $\sigma(-\partial p/\partial x_2 < 0)$.

The standard deviation σ for the conditional averaged pressure gradients is shown in Fig. 7 where σ is defined by

$$\sigma_{\left(-\frac{\partial p}{\partial x_2}\right)} = \sqrt{\overline{\left[\left(-\frac{\partial p}{\partial x_2}\right) - \overline{\left(-\frac{\partial p}{\partial x_2}\right)}\right]^2}} \tag{9}$$

Averaging (overbar) is, again, over the entire (x_1, x_3)-plane. In Fig. 7, the solid lines represent the condition $-\partial p/\partial x_2 > 0$ and the broken lines $-\partial p/\partial x_2 < 0$. Two observations can be made. First the magnitude for the upward directed gradient ($-\partial p/\partial x_2 > 0$) is larger than the magnitude of the

downward directed pressure gradient ($-\partial p/\partial x_2 < 0$). Secondly, the time development over the phase of the conditional averaged gradients in Fig. 6 is similar to that observed for the standard deviation. Moreover, it may also be noted that the standard deviation values are as large as the mean values (Figs. 6 and 7).

IMPLICATION FOR SEDIMENT TRANSPORT

If the bottom was made up of cohesionless sediments, the vertical pressure gradient would generate a force on the sediments moving near the bed. To infer the dynamics of the sediment grains from the computed flow field, since the simulation is carried out for a smooth bed, the bed should behave as a hydraulic smooth bed, even when sediment grains are present. Therefore, there is a limitation for the grain size, d^*, which can be considered. In particular the Reynolds grain number should be small, i.e.

$$\frac{d^* U_{fm}^*}{\nu^*} < \mathrm{O}(10) \tag{10}$$

where U_{fm}^* is the shear velocity.

An estimate of the stabilizing force on the sediment water mixture is submerged weight W (per unit volume) of the mixture

$$W = (\mathrm{s} - 1)(1 - \mathrm{n}) \tag{11}$$

where s is the specific gravity and n the porosity. On the other hand the agitating force F (per unit volume) on the sediment-water mixtures, due to the vertical pressure gradient, can be estimated by means of

$$F = -\frac{\partial \left(\frac{p^*}{\gamma^*}\right)}{\partial x_2^*} \tag{12}$$

where $\gamma^* = \rho^* g^*$, ρ^* being the density of water and g^* the acceleration due to gravity. Assuming that other forces (drag and added mass forces) do not affect the sediment-water-mixture dynamics, the contribution from the vertical pressure gradient compared to the total force needed to move the sediment water mixture. It follows that: a) if the submerged weight is larger than the agitating forces ($W > F$), the sediment do not move in the vertical direction. b) if the submerged weight is smaller than the agitating force ($W < F$), the sediment moves in the vertical direction. Table 2 lists the values of the parameters for selected typical wave periods, and the associated pressure gradients at the bed based on the mean values evaluated at $\omega t = 90°$ from Fig. 6c and from Eq. 11 ($s^* = 2.65$ and $n^* = 0.4$ which are typical values for sediment). The grain size in table 2 is selected such that it satisfies Eq. 10.

Table 2. Typical values of wave periods and the magnitude of the vertical pressure gradient at $\omega t = 90°$. Shields parameter, $\theta = U_{fm}^{*2}/(g^*(s^* - 1)d^*)$.

T^* [s]	d^* [mm]	$\frac{d^* U_{fm}^*}{\nu^*}$ [−]	θ [−]	F [−]	$\frac{F}{W}$ [−]
5	0.22	10	0.60	0.48	0.48
7.5	0.22	8	0.40	0.26	0.26
10	0.22	7	0.20	0.17	0.17
12.5	0.22	6	0.24	0.12	0.12

As listed in Table 2, the sediment size of 0.22 mm (corresponding to medium sand) fulfils the requirement for the smooth bed. Moreover, the Shields parameter is calculated to ensure that all the conditions lead to sediment transport, although the largest period is close to the incipient sediment motion. The vertical pressure gradient is approximated by its average value over the height $\hat{x}_2^*$ equal to d^*, and such that $\hat{x}_2^+ = x_2^* U_{\mathrm{fm}}^* / \nu^*$ is smaller than 10. Taking into account that $U_{\mathrm{fm}}^* / \nu^* = \sqrt{\bar{\tau}_{0\mathrm{m}}} U_{0\mathrm{m}}^* / \nu^*$, it follows that $\hat{x}_2 = \hat{x}_2^* / \delta^*$ is smaller than 0.25. The agitation-force-to-weight ratio F/W is based on the mean value of $(-\partial p / \partial x_2)$ picked up from Fig. 6. However, the instantaneous value of the latter can be as much as twice the mean value, or even larger. Therefore, the F/W ratio in such cases may even exceed unity, implying that even the pressure gradient alone can suspend the sediment grains from the bed.

CONCLUSIONS

1. Turbulent spots can be detected by a criterion involving the strength of the vertical pressure gradient near the bed.
2. The vertical pressure gradient is treated as a turbulence quantity, and classic statistical properties (the mean and the standard deviation) are calculated with conditional averages (depending on whether the gradient is upward or downward directed).
3. The results show that the magnitude of the upward directed conditional averaged pressure gradient is larger than twice the magnitude of the downward directed one.
4. The time scale associated with the fluctuations of the pressure gradient is significantly smaller than that of the velocity fluctuations.

REFERENCES

Blondeaux, P. and G. Vittori. 1994. Wall imperfections as a triggering mechanism for Stokes-layer transition. J. Fluid Mech.264. 107-135.

Carstensen, S., B.M. Sumer, J Fredsøe. 2010. Coherent structures in wave boundary layers. Part 1, J. Fluid Mech. 646. 169-206.

Carstensen, S., B. M. Sumer and J. Fredsøe. 2012. A note on turbulent spots over rough bed in turbulent boundary layers. Physics of Fluids. 24.

Costamagna, P., G. Vittori and P. Blondeaux. 2003. Coherent structures in oscillatory boundary layers. J. Fluid Mech. 474. 1-33.

Jensen, B.L., B.M. Sumer and J. Fredsøe. 1989. Turbulent oscillatory boundary layers at high Reynolds numbers. J. Fluid Mech. 206. 265-297.

Kim, J. and P. Moin. 1985. Application of a fractional step method to incompressible Navier-Stokes equations. Journal of computational physics. 59. 308-323.

Mazzuoli, M., G. Vittori and P. Blondeaux. 2011. Turbulent spots in oscillatory boundary layers. J. Fluid Mech. 685. 365-376.

Mazzuoli, M., 2013. Transition to turbulence in an oscillatory boundary layer and its effects on the motion of a rigid particle. Ph.D. Thesis. University of Genoa. Department of Civil, Chemical and Environmental Engineering.

Orlandi, P. 1989. A numerical method for direct simulation of turbulence in complex geometries. Annual Research Brief. 215. Center for Turbulence Research, Standford University.

Spalart P. R. and B. S. Baldwin. 1987, Direct simulation of a turbulent oscillating boundary layer. NASA Technical Memorandum 89460. Ames Research Center. Moffett Field, California.

Sumer B. M., P. Jensen, L. B. Sørensen, J. Fredsøe, P. F. L. Lui and S. Carstensen, 2010, Coherent structures in wave boundary layers. Part 2. Solitary motion. J. Fluid Mech. 646. 207-231.

Vittori, G. and R. Verzicco. 1998. Direct numerical simulation of transition in an oscillatory boundary layer. J. Fluid Mech. 371. 207-232.